Chem Soc Rev

ROYAL SOCIETY OF CHEMISTRY

TUTORIAL REVIEW

View Article Online
View Journal | View Issue

Cite this: *Chem. Soc. Rev.*, 2022, **51**, 2957

Received 10th December 2021

DOI: 10.1039/d1cs01143j

rsc.li/chem-soc-rev

Metallosupramolecular cages: from design principles and characterisation techniques to applications

Anna J. McConnell

Although metallosupramolecular cages are self-assembled from seemingly simple building blocks, metal ions and organic ligands, architectures of increasingly large size and complexity are accessible and exploited in applications from catalysis to the stabilisation of reactive species. This Tutorial Review gives an introduction to the principles for designing metallosupramolecular cages and highlights advances in the design of large and lower symmetry cages. The characterisation and identification of cages relies on a number of complementary techniques with NMR spectroscopy, mass spectrometry, X-ray crystallography and computational methods being the focus of this review. Finally, examples of cages are discussed where these design principles and characterisation techniques are put into practice for an application or function of the cage.

Key learning points

(1) The directional bonding, symmetry interaction and molecular panelling approaches for the design of metallosupramolecular cages *via* coordination-driven self-assembly.

(2) The complexity of the self-assembly process and the role of factors from building block design (*e.g.* metal ion and ligand geometries), solvent and the presence of templates on the outcome on self-assembly. Thermodynamic and stereochemical considerations are also discussed.

(3) The approach to the characterisation of unknown cages and the use of complementary techniques, such as NMR spectroscopy, mass spectrometry, X-ray crystallography and computational studies.

(4) The implementation of these design principles and characterisation techniques to the design of cages for applications from catalysis to the stabilisation of reactive species.

1. Introduction

Metallosupramolecular cages are a class of molecular containers or flasks[1] that are self-assembled from metal ions and organic ligands by coordination-driven self-assembly exploiting the reversibility of the metal–ligand bond.[2–7] The interest in this class of supramolecular architectures comes not only from the synthetic challenge of their rational design, particularly for cages with increased size and complexity, but also their host–guest chemistry; their well-defined three-dimensional cavities can bind guest molecules, potentially with high affinity and selectivity. Thus, these cages find application in cavity-directed reactions,[1] the stabilisation of reactive species,[8] catalysis,[9] and molecular separations.[10] As a result, the field has evolved from establishing fundamental design principles in pioneering examples of cages[11–14] to designing cages for tailored functionality in applications.

This Tutorial Review will give an introduction to the design principles as well as characterisation techniques for newcomers to the field and furthermore, demonstrate how they underpin the design and characterisation of metallosupramolecular cages for particular applications. For simplicity, metallosupramolecular cages will be referred to as cages throughout the review and while the focus of this review is cages, examples of helicates will also be included to illustrate key points. This Tutorial Review is not intended to be a comprehensive review, but rather illustrate concepts and in particular, highlight recent advances. More comprehensive reviews will be included in each section for readers interested in further information about the topic.

2. Design principles

2.1 Directional bonding, symmetry interaction and molecular panelling approaches

The architectures of many metallosupramolecular cages resemble Platonic or Archimedean solids and different approaches

---

Otto Diels Institute of Organic Chemistry, Christian-Albrechts-Universität zu Kiel, Kiel 24098, Germany. E-mail: amcconnell@oc.uni-kiel.de

have been used to rationally design them from their constituent building blocks, metal ions (M) and organic ligands (L). Three approaches—directional bonding,[6] symmetry interaction[7] and molecular panelling[3]—will be briefly overviewed using a tetrahedron as an example to demonstrate each approach.

In the directional bonding approach described by Stang and co-workers, the three-dimensional cage is described by tritopic and ditopic subunits; for example, a tetrahedron can be broken down into four 60° tritopic (blue) and six 180° ditopic (red) subunits (Fig. 1, top).[6] When the tritopic subunit represents the metal complex on the vertices and the ditopic subunit the ligand on the edges of the tetrahedron, this gives a M_4L_6 tetrahedron. Conversely, a M_6L_4 tetrahedron would result from linear metal complexes (ditopic subunit) on the tetrahedron's edges and tritopic ligand subunits on the vertices.

In the symmetry interaction approach (Fig. 1, middle), Raymond and co-workers defined the symmetry of the cage in terms of the geometric relationship between the metal and ligand, as represented by the coordinate vector (from the interaction between the metal and ligand) and chelate plane (defined by the plane in which the coordinate vectors of the chelating ligands lie).[7] For a M_4L_6 tetrahedron, the three coordinate vectors of each metal complex form a chelate plane containing a C_3 axis and an angle of 70.6° is required between the coordinate vectors within each ligand to bridge the metal centres.

Finally, the molecular panelling approach[3] developed by Fujita and co-workers constructs polyhedral cages from square planar complexes with a 90° angle (achieved by blocking two of the coordination sites with another *cis*-coordinating ligand, *e.g.* ethylenediamine) and 2D panels (*e.g.* triangles, squares and pentagons) representing the organic ligands (Fig. 1, bottom). A M_8L_4 tetrahedron can be designed from four triangular panels and 8 *cis*-protected square planar complexes linked together in an antiparallel fashion.[3] Alternatively, a M_8L_4 cone results from linking the panels together in a parallel fashion.[3]

Anna J. McConnell

Anna McConnell obtained a DPhil under the supervision of Prof. Paul Beer at the University of Oxford. Following postdoctoral research stays at the California Institute of Technology and the University of Cambridge in the groups of Prof. Jacqueline Barton and Prof. Jonathan Nitschke, respectively, she became a Junior Professor at Christian-Albrechts-Universität zu Kiel in November 2016. Her research focuses on stimuli-responsive metal–organic cages, dynamic covalent chemistry and luminescent complexes.

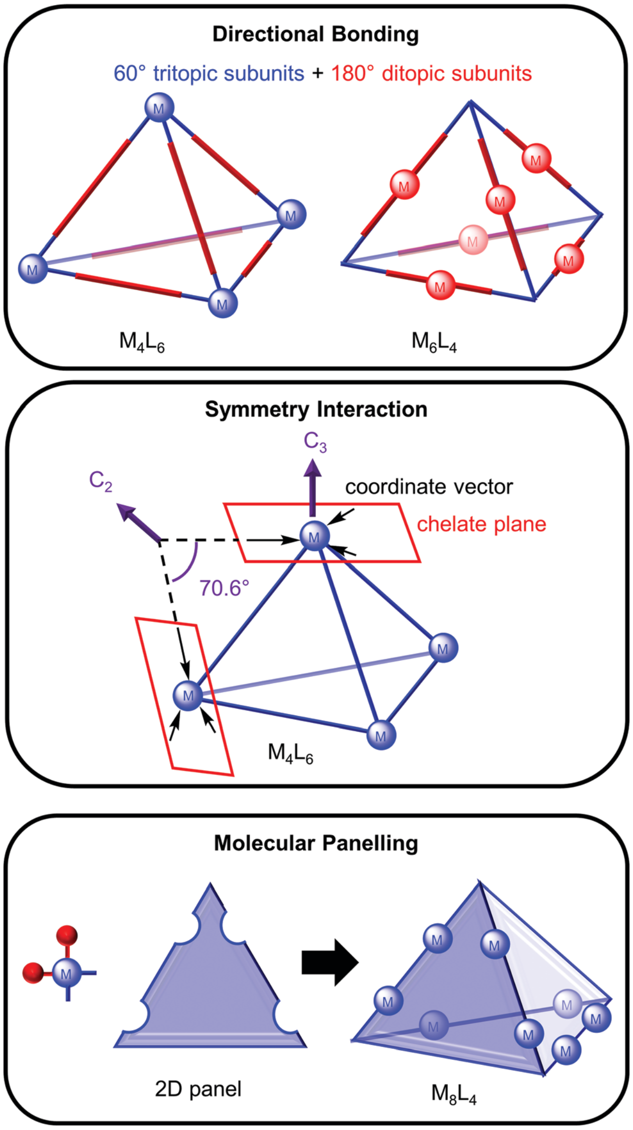

Fig. 1 The design of metallosupramolecular cages by the: (a) directional bonding; (b) symmetry interaction; (c) molecular panelling approaches (for clarity, the red ligands on each metal centre are not shown in the cage).

2.2 Coordination-driven self-assembly of metallosupramolecular cages

Using design principles such as those described in Section 2.1, geometric information for the cage is encoded into the building blocks so that the cage can be self-assembled *via* coordination-driven self-assembly. Highly symmetrical, rigid ligands are typically employed as well as metal ions with predictable coordination geometries since they provide well-defined geometries for the improved rational design of cages.

It is important that the self-assembly process is under thermodynamic control so that the metal–ligand bonds can break and form reversibly; this ensures that error-checking can take place so that the thermodynamically most stable structure(s) results.[7] A subset of coordination-driven self-assembly, subcomponent self-assembly,[2] relies not only the reversible formation of metal–ligand bonds but also dynamic covalent bonds; the ligand, typically a pyridyl imine, forms *in situ* from aldehyde- and amine-functionalised subcomponents templated by the metal ion.

Thus, the choice of metal ion is important not only in terms of its coordination geometry but also its kinetic lability for error-checking during the self-assembly process. For this reason, octahedral (*e.g.* Ga^{III}, Ti^{IV}, Fe^{II}, Co^{II}, Zn^{II}, Cd^{II}, Ni^{II})[2,7] and square planar (*e.g.* Pd^{II} and Pt^{II})[4,5] metal ions are typically used. Lanthanide ions can also be used for self-assembly since they are kinetically labile, however, the variable coordination number and geometry can complicate rational design.[15] Nevertheless, the number of lanthanide-based cages is increasing and various architectures including M_3L_2, tetrahedra, cubes and more recently, a hexameric cage self-assembled from helicates have been reported.[15–17] The counterion of the metal salt can also influence the self-assembly process as a template (see Section 2.2.1) and recently, Reek and co-workers reported halide impurities in metal salts play a catalytic role in the self-assembly of a variety of Pd^{II}, Pt^{II} and Ni^{II} cages;[18] these impurities are proposed to reduce the energy required to convert kinetically trapped species to the thermodynamically favoured cage.

Examples of homometallic cages self-assembled from kinetically inert metal ions, such as Ru^{II} and Ir^{III}, are rarer since self-assembly is under kinetic rather than thermodynamic control, although metal building blocks exploiting the *trans* effect can labilise the metal–ligand bond.[19] To circumvent this problem of kinetic inertness, Lusby and co-workers exploited the kinetic lability of Co^{II} to self-assemble a $Co^{II}_4L_6$ cage that was "locked" through chemical oxidation to the kinetically inert $Co^{III}_4L_6$ cage.[20]

2.2.1 Thermodynamic considerations. The self-assembly process is complex involving multiple equilibria and a variety of factors (*e.g.* metal coordination geometry and kinetic lability, ligand geometry, metal/ligand stoichiometry, concentration, solvent and presence of guests) play a role. Therefore, it can be difficult to predict the outcome since there is a delicate interplay between enthalpy and entropy. The principle of maximum site occupancy[21] states that species where all the metal coordination sites are occupied with ligands are more stable than those with vacant coordination sites since this maximises the number of metal–ligand bonds and therefore, the enthalpy. On the other hand, a system containing a larger number of smaller cages with fewer building blocks is favoured on entropic grounds over one containing a smaller number of larger cages.

In many cases, multiple architectures can be self-assembled from the same building blocks and therefore, various outcomes can be envisaged based on the relative energies of the possible self-assemblies: (a) a single cage when it is the thermodynamically most stable structure; (b) a mixture of cages as the thermodynamic products with the distribution reflecting the relative energies of the cages; (c) a dynamic combinatorial library with a large number of interconverting species in equilibrium. In an interconverting mixture of three architectures in D_2O, Ward and co-workers reported the smaller Co_2L_3 *meso*-helicate and Co_4L_6 tetrahedron were favoured at higher temperature and lower concentration on entropic grounds, whereas the larger $Co_{12}L_{18}$ truncated tetrahedron was favoured at higher concentration and lower temperature (Fig. 2).[22] The hydrophobic effect was proposed to be the driving force for the self-assembly of the larger $Co_{12}L_{18}$ cage in spite of unfavourable electrostatic and entropic effects since the hydrophobic surfaces of the ligand could be more effectively buried away from water. Indeed, the smaller Co_2L_3 helicate predominated following equilibration of the mixture in $MeNO_2$ where the hydrophobic effect is absent (for a more detailed discussion of the solvent effects of water and the hydrophobic effect for self-assembly and host–guest binding see ref. 23 and 24).

Guest binding can also template the self-assembly of cages (Fig. 3). Clever and co-workers reported the addition of 1.5 equivalents of halide ions templated the formation of the $[3X^- \subset Pd_4L_8]^{5+}$ interpenetrated double cage from the $[Pd_2L_4](BF_4)_4$ cage since the smaller halide ions could fit within the binding pockets, whereas the BF_4^- anions were too large.[25]

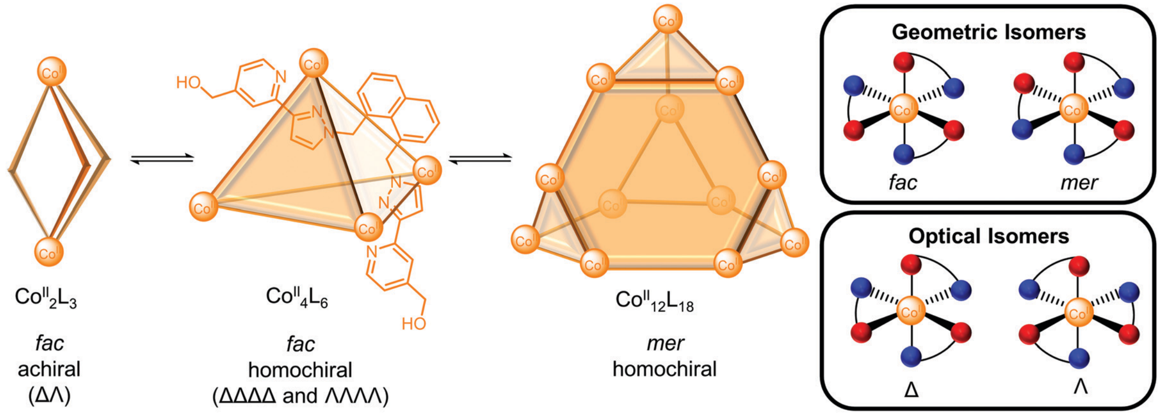

Fig. 2 Mixture of a $Co^{II}_2L_3$ *meso*-helicate, $Co^{II}_4L_6$ tetrahedron and $Co^{II}_{12}L_{18}$ truncated tetrahedron reported by Ward and co-workers where the three architectures result from stereoisomerism of the metal complexes. Inset: Schematic representation of the geometric and optical isomers of individual metal centres where the red and blue balls represent pyridyl and pyrazoyl donor atoms of the cage ligand, respectively.

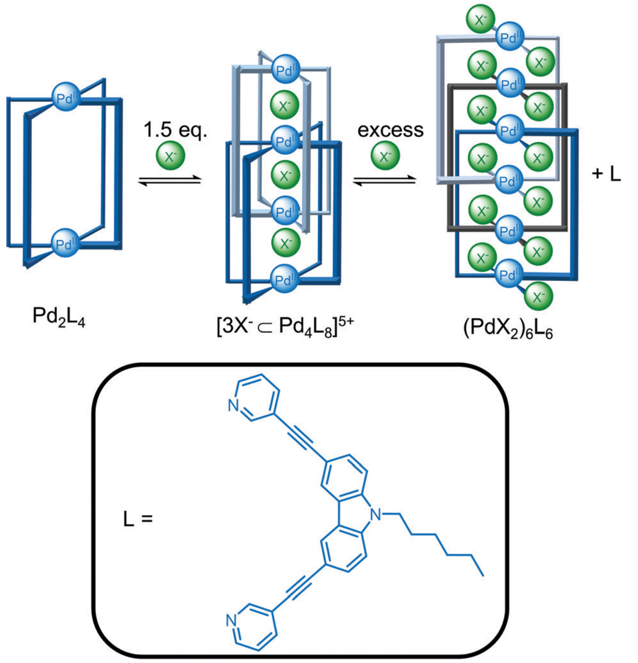

Fig. 3 Clever and co-workers' halide templated formation of a $[3X^- \subset Pd_4L_8]^{5+}$ interpenetrated double cage from a $[Pd_2L_4](BF_4)_4$ cage and subsequent conversion to the triply catenated $(PdX_2)_6L_6$ upon addition of excess halide ions.

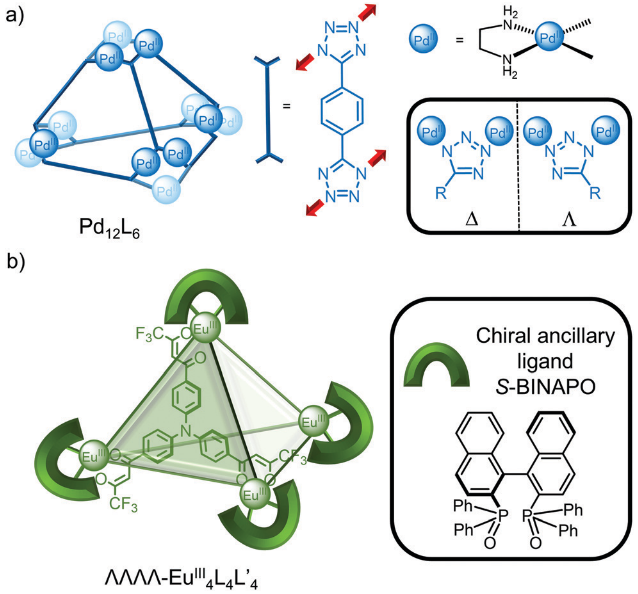

Fig. 4 Homochiral cages: (a) Mukherjee and co-workers' $Pd_{12}L_6$ tetrahedral cage with unusual homochirality due to symmetry breaking of the ligand upon metal coordination in the 1,3-binding mode. Inset: Δ and Λ configurations; (b) Li and Yan's enantiopure $Eu^{III}{}_4L_4L'_4$ cage where the chiral ancillary ligand (L' = *S*-BINAPO) induces the chirality.

The double cage was in equilibrium with the Pd_2L_4 cage and free ligand and addition of excess halide ions to increase conversion resulted, however, in competing coordination of the halide to the metal centre and decomposition of the double cage with release of free ligand. The triply catenated $(PdBr_2)_6L_6$ structure crystallised from the mixture containing excess bromide ions.

2.2.2 **Stereochemical considerations.** The stereochemistry of the metal complexes within cages can lead to different architectures or isomers of the same architecture and have implications for characterisation (see Section 3.1.2).[2] For cages containing octahedral metal complexes with bidentate ligands, the facial (*fac*) and meridional (*mer*) geometric isomers and the Δ and Λ optical isomers need to be considered (Fig. 2, inset). The three different architectures in Fig. 2 are self-assembled from the same building blocks due to different arrangements of the ligands around the metal centres; the metal centres in the *meso*-helicate and tetrahedron are *fac*, whereas those in the truncated tetrahedron are *mer*. Furthermore, the tetrahedron and truncated tetrahedron are homochiral, meaning that all of the metal centres have the same handedness. In contrast, the two metal centres of the *meso*-helicate have opposite chirality and thus, this $\Delta\Lambda$ diastereomer is achiral. Section 3.1.2 contains a more detailed discussion of how different isomers and architectures can be distinguished by NMR spectroscopy on the basis of their symmetry.

While cages based on Pt^{II} and Pd^{II} tend to be highly symmetric due to the square planar coordination and achiral unless a chiral ligand is incorporated, Mukherjee and co-workers recently reported the unusual self-assembly of a homochiral $Pd_{12}L_6$ cage from achiral building blocks (Fig. 4a); symmetry breaking of the ligand upon metal coordination to the 1- and 3-nitrogens of the tetrazole ligand results in either a Δ or Λ configuration (Fig. 4a, inset) with all the metal centres within the cage having the same handedness.[26] Enantiopure cages were self-assembled extending this strategy by using an enantiopure *cis*-blocked Pd complex[27] or through resolution of the enantiomeric cages *via* encapsulation of a chiral guest.[28]

While the stereoselective self-assembly of enantiopure cages[29] often employs enantiopure ligand building blocks, Li and co-workers exploited the variable coordination number of lanthanide metal centres to introduce a chiral ancillary ligand (*S*-BINAPO) to self-assemble the enantiopure cage using an achiral triphenylamine-based ligand (Fig. 4b).[17] Furthermore, exchange of the chiral ancillary ligand for an achiral one resulted in stereochemical memory so that the enantiopure cage was obtained even in the absence of the chiral information.

2.2.3 **Design of large cages.** The self-assembly of large cages[4,30] has gained attention not only for the synthetic challenge but also the potential to encapsulate larger guest molecules, *e.g.* biomolecules such as proteins. Two approaches can be envisaged, each with their own challenges: self-assembly with a smaller number of larger building blocks or alternatively, with a larger number of smaller building blocks. Using the first approach, Severin and co-workers have reported Pd_2L_4 cages with sizes of 3 nm[31] to 4.2 nm[32] and the synthetic challenge of preparing ligands with nanometre-sized lengths was overcome by self-assembling pyridine-functionalised

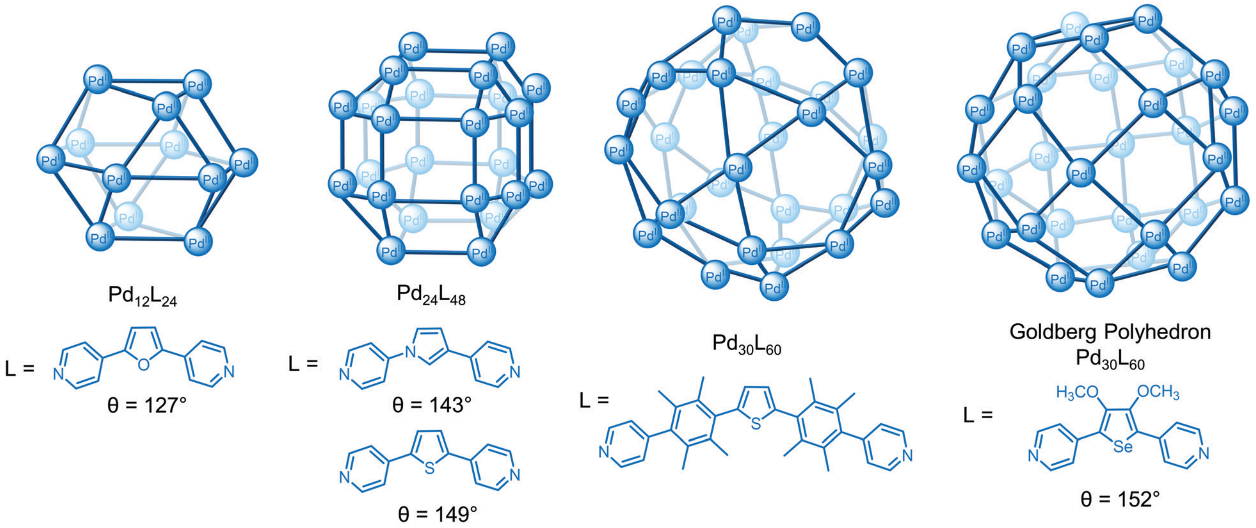

Fig. 5 Series of Pd_nL_{2n} spherical cages reported by Fujita and co-workers where the bend angle (θ) between the donor sites influences the size of the architecture.

clathrochelate-based ligands from a metal salt, dioxime, boronic acid building blocks.[31,32]

Using the second approach, Fujita and co-workers have demonstrated that a series of spherical Pd_nL_{2n} cages[4] of increasing size from the 3.5 nm $Pd_{12}L_{24}$ cuboctahedron[33] to the 8 nm $M_{30}L_{60}$ icosidodecahedron[34] can be self-assembled by tuning the bend angle (θ) between the donor sites in the ligand from 127° to approx. 150° (Fig. 5).[33–35] A key challenge to the successful self-assembly of the $M_{30}L_{60}$ cage was balancing the ligand flexibility; kinetically trapped smaller species self-assembled with more flexible ligands but some flexibility was necessary to overcome the angle mismatch of the 90° square planar complex with the 60° and 108° angles required for the triangular and pentagonal faces, respectively, of the cage.[34] Increasing the bend angle to 152° gave a new class of cage, $Pd_{30}L_{60}$ (Fig. 5) and $Pd_{48}L_{96}$ Goldberg polyhedra with square and triangular faces, rather than the expected $M_{60}L_{120}$ rhombicosidodecahedron.[36]

In a new approach to access larger cages with higher complexity, Domoto and Fujita recently reported that $(M_3L_2)_n$ cages (where n = 2, 4, 6, 8) can be constructed by molecular entanglement where the M_3L_2 building blocks oligomerise *via*

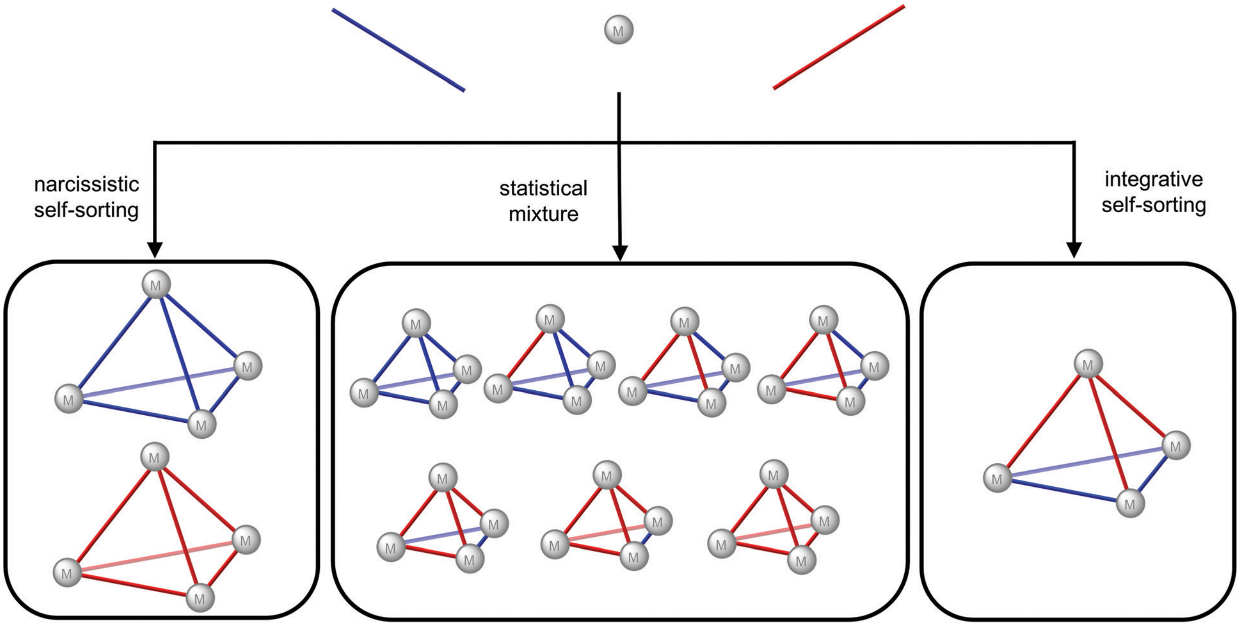

Fig. 6 Outcomes of self-sorting in a self-assembly with metal ions and a mixture of ligands (in red and blue): narcissistic self-sorting; a statistical mixture; integrative self-sorting giving a lower symmetry heteroleptic cage.

metal–acetylene interactions[37,38] and the $(M_3L_2)_8$ truncated cube can be self-assembled from the $(M_3L_2)_2$ cage by anion exchange of BF_4^- for NO_3^-.[37] In a similar hierarchical self-assembly approach, Sun and co-workers reported $Eu^{III}{}_2L_3$ helicates self-assemble into a hexameric cage with a 4 nm diameter in the presence of anions.[16]

2.2.4 Design of lower symmetry cages. While the majority of cages are highly symmetric due to the increased ease of rational design, the number of lower symmetry cages is ever increasing and several strategies have been adopted to reduce symmetry within the cage: (a) symmetry breaking of the ligand upon metal coordination, analogous to that described in Section 2.2.2 for the self-assembly of homochiral cages; (b) self-assembly of heteroleptic cages containing multiple ligands; (c) use of non-symmetric ligands to form homoleptic but lower symmetry cages; (d) use of multiple metals to form heterometallic cages. This section will focus on strategies (b–d) and the role of self-sorting.[39]

For self-assembly with a mixture of ligands, three outcomes can be envisaged based on the self-sorting, or lack thereof (Fig. 6): narcissistic self-sorting giving homoleptic cages with one ligand type in each cage; a statistical mixture where both ligands are incorporated into the cages according to their statistical distribution; integrative self-sorting where a non-statistical distribution of heteroleptic cages results. The key challenges to the design of heteroleptic cages *via* integrative self-assembly[40] are, therefore, stabilisation of the heteroleptic cage/s relative to the homoleptic cages and biasing the system away from the statistical mixture. Various strategies have been successfully employed including the use of templates, steric effects, complementarity of the ligands' geometries, ligand interactions and control of the metal's coordination sphere.[40]

Severin and co-workers exploited a selection approach to identify heteroleptic cages by screening six ligands with a sub-stoichiometric amount of a Pd salt in a virtual combinatorial library;[41] although a large number of species are theoretically possible, the most thermodynamically stable self-assemblies were selected by competition for the metal salt. Using this approach, the $Pd_6L_6L'_6$ cage with an unusual trigonal antiprismatic architecture was identified, even though none of the ligands screened form hexanuclear cages and ligands L and L′ form Pd_4L_8 and $Pd_{12}L'_{24}$ homoleptic cages, respectively (Fig. 7a).

Non-symmetric ligands have also been used to access lower symmetry cages and similar approaches such as the use of templates and ligand geometry complementarity have been exploited to induce integrative self-sorting.[42] Yuasa and co-workers reported the self-assembly of an open Pd_2L_4 cage from a ligand containing pyridine and imidazole binding sites.[43] Despite the three potential conformations of the two coordination motifs (perpendicular, parallel and antiparallel) and four possible isomers for the open cage depending on the relative orientations of the ligand in the parallel conformation, only one isomer formed (Fig. 7b); DFT calculations revealed this isomer was 61–204 kcal mol^{-1} more stable than the other isomers.

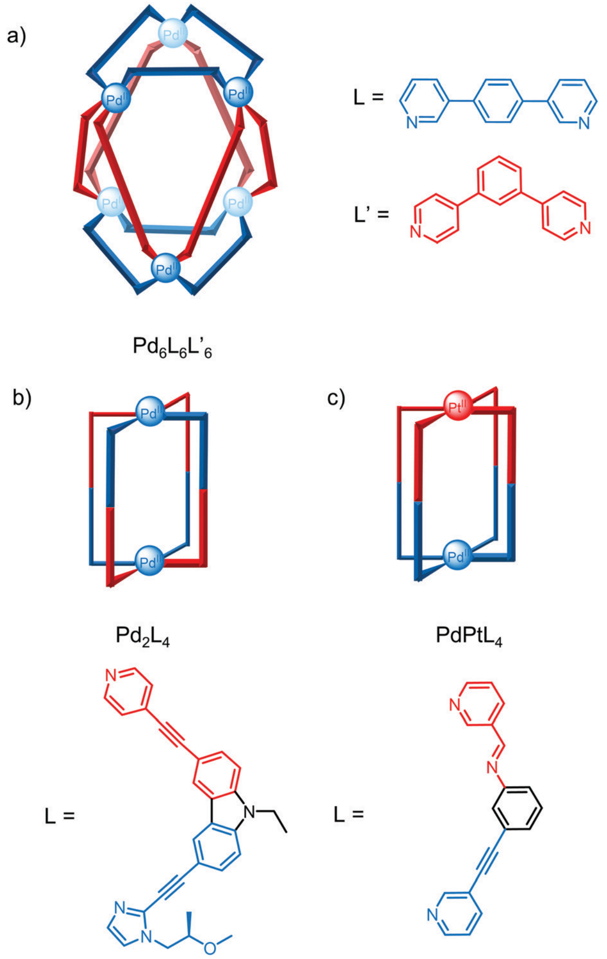

Fig. 7 Approaches to lower symmetry cages: (a) Severin and co-workers' heteroleptic $Pd_6L_6L'_6$ cage with two different ligands; (b) Yuasa and co-workers' homoleptic Pd_2L_4 cage with non-symmetric ligands containing two coordination motifs; (c) Crowley and co-workers' $PdPtL_4$ heterobimetallic cage with an asymmetric cavity.

The self-assembly of heterometallic cages relies on the different coordination preferences of the metals and while there are a number of examples of heterometallic cages, the majority have symmetric cavities.[44,45] Crowley and co-workers recently reported a rare example of a lower symmetry heterobimetallic $PdPtL_4$ cage where guest binding induces loss of the cage's four-fold symmetry and desymmetrisation of the 2,6-diaminoanthraquinone guest (Fig. 7c).[46]

3. Characterisation techniques

While the cage architecture can, in many cases, be successfully predicted using the design principles above (see Section 2), this is not always the case given the complexity of the self-assembly process. This section will introduce the approach for characterising and identifying an unknown cage(s) and studying its host–guest chemistry, discuss recent technique advances/developments as well as highlight challenges to characterisation.

Characterisation[47] is reliant on a number of techniques and this section will focus on the three most commonly used techniques—NMR spectroscopy, mass spectrometry (MS) and X-ray crystallography—since these provide complementary information; NMR spectroscopy reveals the symmetry of the resulting self-assembled architecture(s) through the number of ligand environments, mass spectrometry the stoichiometry of the metal ion and organic ligand building blocks and X-ray crystallography the 3-dimensional connectivity of the building blocks within the cage. Finally, advances in computational methods for aiding cage characterisation and design will be discussed.

3.1 NMR spectroscopy

There are a number of excellent reviews on the NMR characterisation of supramolecular structures in general.[47–50] This section will be divided into the NMR characterisation of the: (a) self-assembly process; (b) resulting cage(s); (c) host–guest chemistry.

3.1.1 Characterisation of the self-assembly process. Given the outcome of self-assembly depends on a number of factors (see Section 2.2.1), small scale self-assembly experiments are often performed in deuterated solvents since this not only facilitates screening of a number of self-assembly conditions, but the self-assembly process can be simultaneously monitored *in situ* by NMR spectroscopy until there are no further changes to the NMR spectra. This indicates the system has either reached thermal equilibrium (in the case of a system under thermodynamic control) or reached a metastable state (in a system under kinetic control). While *in situ* monitoring by NMR spectroscopy allows the characterisation of any resulting cage(s), partially formed cages and other transiently formed species are difficult to characterise since they are likely to be lower symmetry species and form in low concentration for short periods of time.

Nevertheless, Hiraoka and co-workers have developed an NMR-based method, quantitative analysis of self-assembly process (QASAP),[51] to indirectly quantify these species over time by monitoring the NMR-detectable species (free ligand, cage and metal containing a ^{1}H NMR active ligand such as pyridine). QASAP as well as NASAP (numerical analysis of self-assembly process)[52] also developed by Hiraoka and co-workers, have been used to provide insight into the self-assembly pathway of cages under thermodynamic and kinetic control; in the self-assembly of a Pd_6L_8 cage, QASAP revealed the final intramolecular ligand exchange of pyridine (Py) in $[Pd_6L_8Py_1]^{12+}$ was the rate-determining step with further evidence from the detection of this species by mass spectrometry.[51]

3.1.2 Characterisation of cages. Once the self-assembly process is complete, characterisation by NMR spectroscopy is exploited to determine the number of species present and identify the resulting cage architecture(s). The choice of metal ion in the self-assembly influences not only NMR data acquisition but also interpretation; for self-assemblies incorporating diamagnetic metals such as Zn^{II}, Pt^{II} and low spin Fe^{II}, the full suite of 1D (*e.g.* ^{1}H, ^{13}C, ^{19}F, ^{31}P) and 2D (*e.g.* COSY, DOSY, NOESY, ROESY, HSQC and HMBC) NMR techniques are available. Structural information can be readily extracted from the chemical shift, integrals and coupling constants *etc.* However, characterisation can be more challenging when mixtures of cages or lower symmetry cages with multiple ligand environments are present since there is an increased chance of signal overlap in the relatively narrow diamagnetic NMR region. There is the potential, however, to exploit pure-shift NMR methods to simplify the analysis through suppression of coupling.[53]

In contrast, the shortened relaxation times from the presence of paramagnetic metal centres such as Co^{II}, Ni^{II} and high spin Fe^{II} limits the number of NMR techniques for characterisation. Furthermore, the structural information cannot be as readily extracted since: (a) the NMR signals can be found over a much wider chemical shift range due to large paramagnetic shifts; (b) integration is less reliable when there is non-uniform excitation over this wider chemical shift range; (c) the NMR signals have broad linewidths, resulting in loss of the coupling information; (d) in some cases, signals with very short relaxation times and/or broad linewidths can be missing entirely (Fig. 8).[54,55] On the other hand, the shorter relaxation times allow the acquisition of more scans in a shorter amount of time from reduction of the acquisition times and recycle delays and this can lead to increased sensitivity.[54,56,57]

Previously, the above challenges often limited characterisation of paramagnetic cages to ^{1}H NMR spectroscopy only or in some cases, assignment using the Solomon equation, which relates T_1 relaxation times to metal–proton distances from an X-ray crystal structure (see Section 3.3 for challenges with obtaining these).[56,57] However, McConnell and co-workers recently optimised a paramagnetic NMR toolbox that enables detailed structural characterisation of paramagnetic cages in solution using a combination of 1D (*e.g.* ^{1}H, proton-coupled ^{13}C, selective ^{1}H decoupling ^{13}C, steady state NOE) and 2D (COSY, NOESY and HMQC) NMR techniques.[54] While its use is still in its infancy with application to the characterisation of highly symmetric tetrahedral cages thus far (Fig. 8), optimisation studies using mononuclear complexes demonstrated its

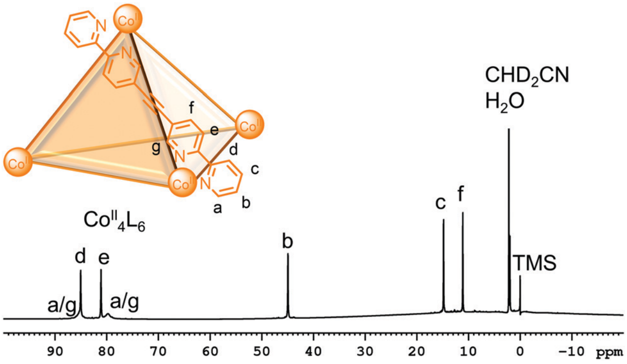

Fig. 8 ^{1}H NMR spectrum of a Co$^{II}_4$L$_6$ cage showing the characteristic large paramagnetic shifts and broad linewidths resulting from the presence of paramagnetic centres. The assignments were made using the paramagnetic NMR toolbox reported by McConnell and co-workers. Adapted with permission from ref. 54. Copyright 2020 Wiley-VCH.

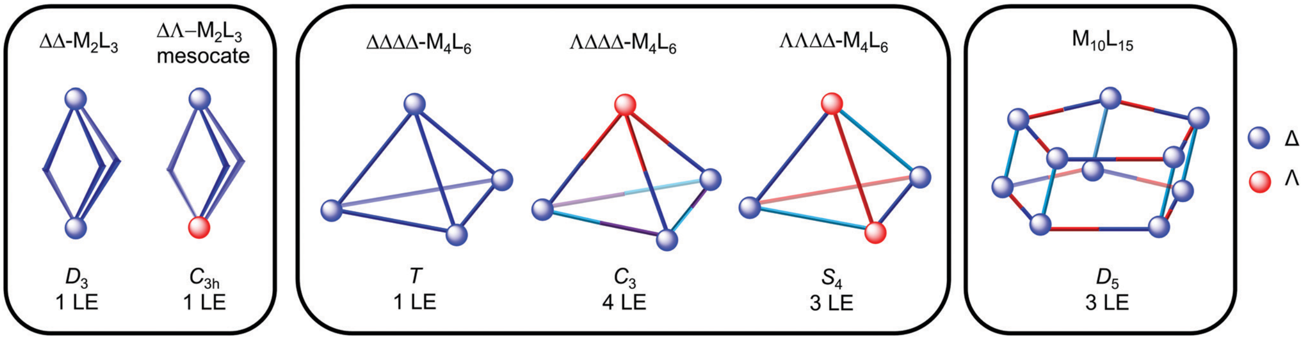

Fig. 9 Representations of M_2L_3, M_4L_6 and $M_{10}L_{15}$ architectures with symmetric ligands showing the idealised symmetry and expected number of ligand environments (LE), as represented by the different colours.

potential for the characterisation of more complex systems (*e.g.* mixtures of cages or lower symmetry cages).[54]

Analysis of the 1D and 2D NMR data indicates whether a discrete cage, mixture of cages or a dynamic combinatorial library result from the self-assembly. In the case of a discrete cage or a mixture of cages, analysis provides information about the symmetry of the resulting self-assembled architecture(s) through the number of ligand environments. This combined with a knowledge of the design principles (see Section 2) can allow proposal of the cage architecture(s).

Fig. 9 shows the idealised symmetry of M_2L_3, M_4L_6 and $M_{10}L_{15}$ architectures and corresponding number of ligand environments (LE), provided the ligand is symmetric and there is no symmetry breaking upon coordination. The T-, C_3- and S_4-diastereomers of M_4L_6 tetrahedra can be differentiated on the basis of the number of ligand environments (1, 4 and 3, respectively). Furthermore, cages containing *mer* octahedral metal complexes such as the $Co_{12}L_{18}$ truncated tetrahedron[22] (Fig. 2) and $M_{10}L_{15}$ pentagonal prism (Fig. 9) have three ligand environments, whereas the T-symmetric M_4L_6 tetrahedron with *fac* octahedral complexes only has one. Highly symmetrical architectures often result since highly symmetrical building blocks are typically used and multiple architectures with the same number of ligand environments could be possible from the same building blocks *e.g.* a M_2L_3 helicate and T-symmetric M_4L_6 tetrahedron, each with one ligand environment. Thus, these architectures cannot be distinguished on the basis of NMR spectroscopy alone and other techniques, such as mass spectrometry and X-ray crystallography, are necessary (see Sections 3.2 and 3.3).

Diffusion ordered spectroscopy (DOSY) can be useful in these circumstances and for general characterisation since it provides information about the size and shape of the cage.[48] Firstly, DOSY indicates whether the signals assigned to the cage have the same diffusion coefficient and therefore, most likely belong to the same species. This caveat is necessary since architectures with similar molecular weights can be difficult to distinguish by DOSY, particularly when their chemical shifts are similar and in this case, a 2–3 fold difference in diffusion coefficient is recommended.[49] For example, Fujita's Goldberg polyhedral $M_{30}L_{60}$ (Fig. 5) and $M_{48}L_{96}$ cages could not be separated by DOSY since the signals of the two species were broad and overlapping.[36]

Secondly, the diffusion coefficient obtained from DOSY can be used to give an estimation of the cage's size. For example, the $Pd_{24}L_{48}$ cage in Fig. 5 ($\log D = -10.49$) has a smaller diffusion coefficient than the smaller $Pd_{12}L_{24}$ cage ($\log D = -10.3$).[35] The hydrodynamic radius of the cage can be calculated from the diffusion coefficient using the Stokes–Einstein equation.[48] This equation assumes a hard sphere is diffusing in a continuum fluid and the contributions from solvent and ion-pair interactions are neglected. While these approximations appear valid for spherical cages, they may not be for non-spherical cages. In those cases, the modified Stokes–Einstein equation is more appropriate since it takes into account shape and size factors.[48]

The use of DOSY has been largely limited to diamagnetic rather than paramagnetic cages due to the large paramagnetic shifts and broad linewidths. However, the recent report of paramagnetic DOSY for first row transition metal complexes by Byers and co-workers[55] demonstrates the potential for more widespread use of DOSY for paramagnetic cages. Indeed, the hydrodynamic radius determined by DOSY for a trigonal bipyramidal cage incorporating iron in three different spin states reported by Riddell and co-workers showed good agreement with the diameter obtained from the X-ray crystal structure.[58]

3.1.3 Characterisation of host–guest chemistry. Once a cage has been identified, its host–guest chemistry can also be investigated by NMR spectroscopy and association constants can be determined from NMR titration studies. While a detailed discussion of this method falls beyond the scope of this review, further information can be found in the review by Thordarson.[59] Instead, this section will focus on NMR techniques that provide evidence for encapsulation, including DOSY and chemical exchange saturation transfer (CEST)[60] NMR methods.

Initial evidence for encapsulation comes from changes to the chemical shifts of the cage as well as guest signals. These shifts can be observed by ^1H NMR spectroscopy but also other types of NMR spectroscopy when the guest and/or cage contain NMR active nuclei such as ^{19}F and ^{31}P. Two situations can be envisaged based on the rate of guest exchange compared to the

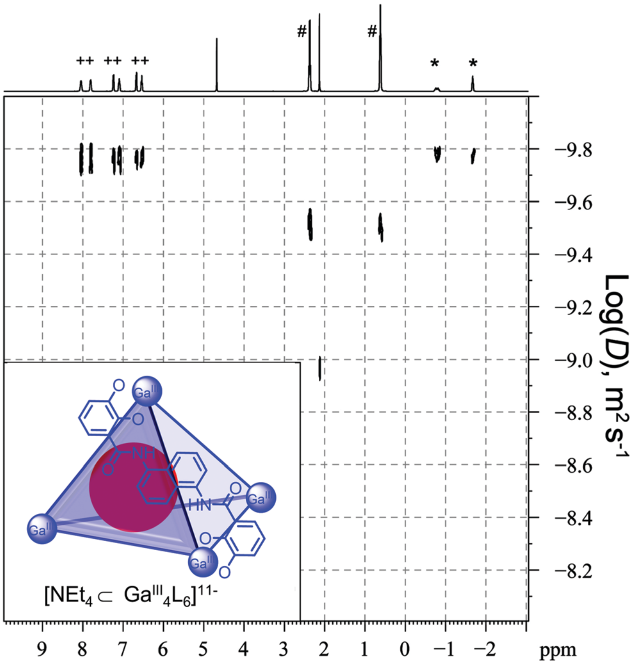

Fig. 10 ^{1}H and DOSY spectra of Raymond's [NEt$_4$⊂Ga$^{III}_4$L$_6$]$^{11-}$ host–guest complex where the encapsulated NEt$_4^+$ guest is in slow exchange with "free" NEt$_4^+$. Signals marked with + correspond to the cage, * the encapsulated NEt$_4^+$ guest and # the "free" NEt$_4^+$. Adapted with permission from ref. 62. Copyright 2008 American Chemical Society.

NMR time-scale: slow exchange where two sets of signals are observed, corresponding to the empty cage (or alternatively, the free guest) and host–guest complex; fast exchange so only one set of signals is observed reflecting the average of the empty cage and host–guest complex signals.

The magnitude of the chemical shift changes upon guest encapsulation is dependent on a number of factors since not only the ligand but also the metal can influence the environment of the cavity. In many cases, the cavity is enclosed by ligands containing aromatic groups. Therefore, guest signals typically shift upfield as a result of shielding, reflecting the weaker field the guests experience compared to the applied magnetic field.[61] For example, the signals of encapsulated NEt$_4^+$ (marked with *) within the Ga$^{III}_4$L$_6$ tetrahedral cage reported by Raymond and co-workers are in slow exchange and shifted compared to the "free" guest (marked with #, Fig. 10).[62] In contrast, Nitschke and co-workers recently reported a Fe$^{II}_4$L$_6$ tetrahedral cage containing antiaromatic walls and the signals of polyaromatic hydrocarbon guests were observed to shift up to 15 ppm downfield due to deshielding.[61]

Large shifts of the guest signals upon encapsulation are also observed with paramagnetic cages, facilitating detection of host–guest binding.[56,57] Furthermore, the potential for increased scanning due to the shorter relaxation times can lead to improved sensitivity. For example, Nitschke and co-workers reported trace impurities of *cis*-decalin in a sample of commercial *trans*-decalin could be detected through the formation of its host–guest complex with a high spin Fe$^{II}_4$L$_4$ tetrahedral cage.[57]

For host–guest complexes in slow exchange, DOSY can provide further evidence for guest encapsulation since the cage and encapsulated guest will have the same diffusion coefficient that is distinct from the "free" guest (Fig. 10). The observed diffusion coefficients, however, can be affected by ion-pairing with Raymond and co-workers reporting a decrease in the diffusion coefficient of a Ga$^{III}_4$L$_6$ cage with an increasing amount of the NEt$_4^+$ guest but addition of a second counter-cation K$^+$ disrupted ion-pairing leading to an increase of the diffusion coefficient for "free" NEt$_4^+$.[62]

Chemical exchange saturation transfer (CEST)[60] NMR methods can be used to study host–guest systems in slow exchange, particularly when there is line broadening of the NMR signals from exchange and undetectable signals due to weak guest binding.[50] In a CEST experiment the bound guest is selectively "labelled" with a saturation pulse so that it has no magnetisation. Since these "labelled" bound guests exchange with the free guest population, the signal for the free guest decreases in intensity. Thus, CEST techniques can amplify the signal of the lower concentration species (the host–guest complex), which may not be detectable, by exploiting the sensitivity of the higher concentration species (the free guest).

Despite its increased sensitivity, there are relatively few examples of CEST experiments for characterising the host–guest complexes of cages. ^{129}Xe hyper-CEST experiments increase the sensitivity of detection by combining hyperpolarisation and CEST with Dmochowski and co-workers reporting that a [Xe⊂Co$_4$L$_6$]$^{4-}$ host–guest complex could be detected at a concentration of 100 pM.[63] Furthermore, hyper-CEST enabled detection of a mixture of [Xe⊂Co$_n$Fe$_{4-n}$L$_6$]$^{4-}$ host–guest complexes when these species could not be simultaneously measured directly by hyperpolarised ^{129}Xe NMR spectroscopy due to weak signals and exchange between the different species (Fig. 11).[64]

Although it has yet to be applied to the characterisation of metallosupramolecular cages, an emerging new tool in the detection of host–guest interactions by CEST is ^{19}F guest exchange saturation transfer (GEST) reported by Bar-Shir and co-workers since it can amplify undetectable host–guest complex signals and quantify guest exchange.[50] Furthermore, various guest molecules incorporate a ^{19}F atom and thus, the guest is not restricted to Xe like hyper-CEST.

3.2 Mass spectrometry

For a general introduction to instrumentation and the study of supramolecules by mass spectrometry, the reader's attention is turned to reviews by Schalley.[65,66] For metallosupramolecular cages, mass spectrometry provides complementary information to NMR spectroscopy regarding the number of each building block within the structure and this can confirm the type of architecture proposed from the symmetry observed by NMR spectroscopy. There are a number of caveats, however, when comparing information obtained from mass spectrometry and NMR spectroscopy. Firstly, the mass spectrometric measurements take place at much lower concentrations (typically μM range) than NMR spectroscopy and thus, other species

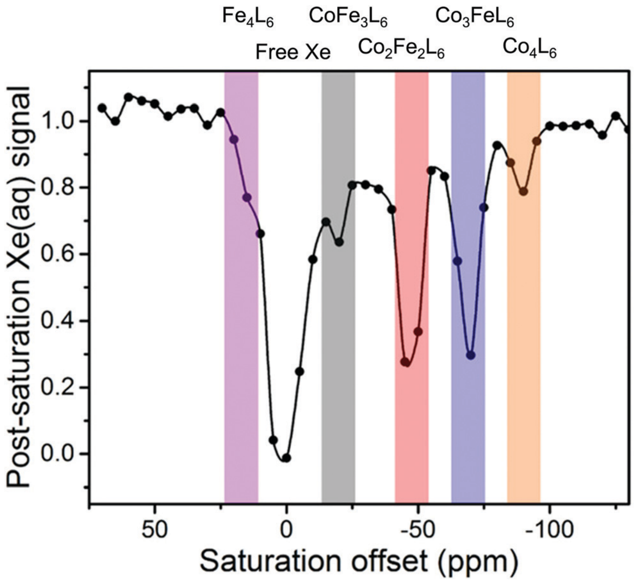

Fig. 11 CEST spectrum reported by Dmochowski and co-workers of a mixture of $[Xe\subset Co_nFe_{4-n}L_6]^{4-}$ host–guest complexes detected using hyperCEST. Adapted with permission from ref. 64. Copyright 2020 American Chemical Society.

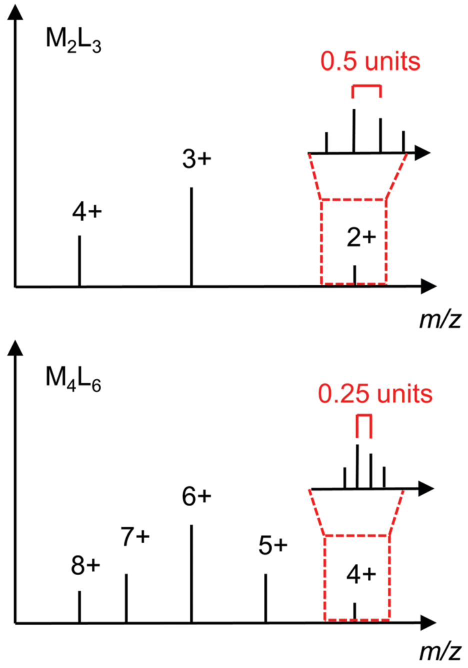

Fig. 12 Idealised mass spectra of M_2L_3 and M_4L_6 structures showing how they can be differentiated on the basis of the series of ion peaks and isotope pattern for a particular *m*/*z* ratio.

including fragments may be present in the more dilute sample due to the change in the equilibrium. Secondly, mass spectrometric measurements take place in the gas phase where the cage is no longer solvated and in equilibrium with its constituent building blocks and therefore, different properties of the cage may be observed in the gas phase *versus* solution.[65] Finally, the intensity of the peaks in the mass spectrum does not correlate with their concentration.[65] Therefore, NMR assignment of signals to a particular architecture in a mixture of cages cannot be made on the basis of the relative peak intensities of the architectures in the mass spectrum.

Cages are typically characterised by electrospray ionisation (ESI) mass spectrometry since this uses relatively mild ionisation conditions.[66] Nevertheless, characterisation can be challenging due to the relatively weak metal–ligand coordinative bonds; the cages can be prone to fragmentation under not only the ionisation conditions (*e.g.* heat from the desolvation chamber) but also due to the low μM concentration. Increased concentrations (100–300 μM) can lead to spectra with fewer fragments, although this is at the expense of increased ion source cleaning.[66] For particularly labile cages where ESI mass spectrometry is not suitable, Yamaguchi, Fujita and co-workers have reported coldspray ionisation (CSI) mass spectrometry as a variant of ESI mass spectrometry where both the cage solution and ion source are cooled to reduce fragmentation.[67]

3.2.1 Characterisation of cages. Provided the cage remains intact during the measurement, the mass spectrum of a cage has a number of features that can be used to identify/confirm the architecture (Fig. 12). Firstly, the mass spectrum will consist of a series of ion peaks at different *m*/*z* ratios for the different charged states of the cage, *e.g.* from 1+ to *n*+ following loss of up to n counteranions for a positively charged cage. Secondly, the isotope pattern of a particular ion peak can be used to determine its charge, *n*.

Mass spectrometry is particularly important for determining the composition of cages that cannot be differentiated on the basis of their NMR spectra alone, *e.g.* a $[M_2L_3]^{4+}$ helicate and *T*-symmetric $[M_4L_6]^{8+}$ tetrahedron (see Section 3.1.2). Fig. 12 shows idealised mass spectra for these two architectures to illustrate how they can be distinguished; while there are several ion peaks in common (*i.e.* at the same *m*/*z* ratio), the ion peaks corresponding to the odd charges of the M_4L_6 are not present for the M_2L_3. Furthermore, the difference in charge is evident in the isotope patterns with a spacing of 0.5 units and 0.25 units for the $[M_2L_3]^{2+}$ and $[M_4L_6]^{4+}$, respectively.

Mass spectroscopy can, however, provide more information than just the number of each building block within a cage and techniques such as tandem MS/MS[65,66] and ion mobility mass spectrometry[66,68,69] also play a role in the characterisation of cages and their host–guest complexes. While the discussion thus far has pointed out the challenges associated with characterisation due to undesired cage fragmentation, tandem MS/MS experiments exploit fragmentation of a mass-selected ion peak of the cage to provide additional structural information. For example, Schalley, Nitschke and Sanders used infrared-multiphoton dissociation experiments to distinguish specific from non-specific binding of crown ethers (C) in a $Fe_4L_6C_6$ tetrahedral polycatenane by comparing the fragmentation of the $[Fe_4L_6C_6]^{8+}$ and $[Fe_4L_6C_7]^{8+}$ ions, respectively.[70]

Ion-mobility mass spectrometry selects ions based on their *m*/*z* ratio and separates them according to their collision cross section in a drift tube with a low electric field; the collision

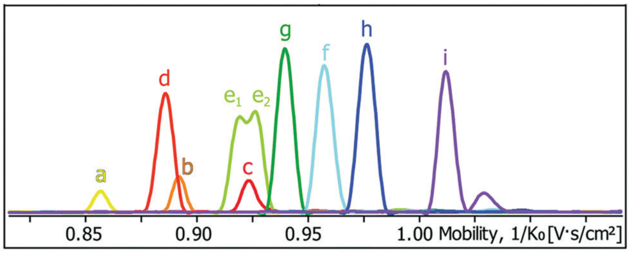

Fig. 13 Mobilogram of a mixture of 10 heteroleptic cages (a–i) reported by Clever and co-workers depicting the differentiation of the cages on the basis of their collision cross section (increasing from left to right) by trapped ion mobility mass spectrometry. Reproduced from ref. 71 with permission from the Royal Society of Chemistry.

cross section is used as a measure of the ion size and ions with larger collision cross sections undergo more collisions, resulting in longer arrival times at the detector. Thus, ion-mobility mass spectrometry can be used to separate ions with the same *m*/*z* ratio but different sizes. This is particularly useful when cages cannot be distinguished by other techniques, such as NMR spectroscopy. For example, Clever and co-workers demonstrated that 10 heteroleptic cages a–i including two isomeric cages generated from Pd^{II} ions and four different ligands could be differentiated by their collision cross sections (Fig. 13).[71]

3.2.2 Characterisation of host–guest complexes. Host–guest complexes can also be characterised by mass spectrometry using similar methods to those described in Section 3.2.1. The series of ion peaks for the host–guest complex will be shifted to different *m*/*z* ratios *versus* the empty cage and compared with NMR spectroscopy, the stoichiometry of guest binding can be determined more straightforwardly when multiple guests are encapsulated. Furthermore, ion-mobility MS can provide information about changes to the cage's shape upon guest encapsulation.

3.3 X-Ray crystallography

X-Ray crystallography is a powerful characterisation technique, providing the three-dimensional connectivity of the metal ions and ligands within a cage and in some cases, evidence of guest encapsulation. Given the nanomolecular size of cages, there are a number of challenges associated with obtaining a single crystal of sufficient quality that diffracts well in addition to refining the crystal structure due to disorder from the cage, solvent, guest molecules and counterions.[72] Numerous crystallisation conditions are typically screened to obtain suitable crystals and synchrotron radiation is used in many cases to improve the resolution for weakly diffracting crystals.

Despite these challenges, X-ray crystallography is instrumental in the characterisation of cages, particularly for those where other techniques give ambiguous structural assignments or cannot be used. For example, the Goldberg polyhedral $Pd_{48}L_{96}$ cage could not be distinguished from the smaller Goldberg polyhedral $Pd_{30}L_{60}$ cage by DOSY (see Section 3.1.2) or be detected by mass spectrometry.[36] While both cages crystallise, a single crystal X-ray structure with 2.85 Å resolution was obtained of the $Pd_{48}L_{96}$ cage by collecting data for more than 10 crystals with different cell parameters to the $Pd_{30}L_{60}$ cage.

Since crystallisation is driven by solubility and crystal packing effects, the X-ray structure does not necessarily reflect the major species in solution as it is determined from a single crystal in the solid state. Bloch and co-workers recently demonstrated that three isomers of a cage can be selectively crystallised *via* self-sorting from a dynamic combinatorial library and DFT calculations revealed that the crystallised isomers were not the thermodynamically most stable isomer.[73]

The crystallisation of host–guest complexes has the additional challenge that crystals of the cage can be obtained with solvent in the cavity rather than the guest or the guest is too disordered to model in the X-ray crystal structure of the host–guest complex.[74] Ward and co-workers have reported improved crystallisation of host–guest complexes using Fujita's "crystalline sponge" method[75] where crystals of the cage are soaked in the guest rather than crystallising the cage from solution in the presence of the guest.[74]

Surprisingly, X-ray crystal structures of 1 : 2 host–guest complexes of a Co_8L_{12} cage were obtained where the guests occupy up to 87% of the cage's cavity volume (Fig. 14) when solution studies indicated the formation of a 1 : 1 host–guest complex.[74] This apparent violation of the Rebek 55% rule for optimal binding is attributed to the use of a large excess of guest (*i.e.* non-equilibrium conditions) and favourable interactions, such as π–π stacking between guests and hydrogen bonding between the guest and cage. Furthermore, solution experiments at higher concentrations also indicated the formation of the 1 : 2 host–guest complex, showing the importance of using complementary techniques.

3.4 Computational studies

Computational studies are playing an increasingly large role in both the design and characterisation of metallosupramolecular

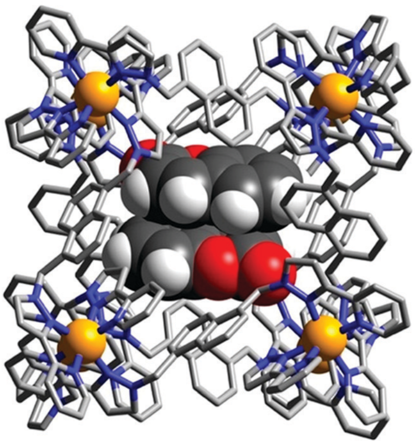

Fig. 14 X-Ray crystal structure of $[(\text{coumarin})_2{\subset}Co_8L_{12}]^{16+}$ reported by Ward and co-workers where the cage is depicted as a wireframe and the two guests in spacefilling. Reproduced with permission from ref. 74. Copyright 2020 Wiley-VCH.

cages. Duarte and co-workers reported *cgbind*, an open source Python module and web app, for generating three-dimensional structures of cages from their metal ion and organic ligand building blocks, predicting binding affinities for guests and calculating properties of the cages such as their electrostatic potential, cavity size and pore size.[76] Furthermore, it has been applied to provide insight into the catalytic activity of a Pd_2L_4 cage (see Section 4).[77]

Lewis and Jelfs have recently proposed a high-throughput screening method employing the supramolecular toolkit (stk) for identifying low-symmetry Pd_2L_4 cages.[78] The potential of this approach to facilitate cage discovery was demonstrated through the screening of 60 unsymmetrical ligands for the energies of the four possible Pd_2L_4 isomers and 5 ligands were identified for synthetic experiments; of these, four self-assembled into a single isomer of a heteroleptic cage, whereas one produced a mixture of isomers.

Computational methods also have the potential to make the host–guest screening more efficient. Using the protein/ligand docking GOLD program, Ward, Hunter and co-workers optimised a scoring function for a water soluble Co_8L_{12} cage using a dataset of experimental binding affinities and *in silico* screening of a library of 3000 guests identified 15 previously unknown guests, predicting their binding affinities within an order of magnitude.[79] It is proposed this approach can be applied to other rigid cages and for host–guest binding in solvents other than water, provided there is an X-ray structure/model of the cage and a large enough dataset of experimental binding affinities for optimising the scoring function.[79]

4. Applications

Metallosupramolecular cages are employed in a variety of applications including exploiting the confined space within the cavity for modulating the properties of encapsulated molecules. Given the breadth of applications from catalysis to molecular separations, it is not possible to give a detailed description and therefore, this section will focus on three examples to illustrate the synergy between design (Section 2) and characterisation techniques (Section 3) in the development of cages for tailored functionality in applications.

Reactive species can be stabilised upon encapsulation and subsequently released exploiting the host–guest chemistry of the cage. Yoshizawa and co-workers reported the photochemical stability of the radical initiator 2,2′-azobisisobutyronitrile (AIBN) is increased by >380 times when bound within a Pd_2L_4 cage due to light absorption by the ligands' large aromatic panels (Fig. 15).[80] Host–guest complex formation was confirmed by mass spectrometry and the methyl protons of AIBN were observed to desymmetrise and shift significantly upfield by almost 4 ppm upon encapsulation. The X-ray crystal structure also revealed the S-shaped *trans* configuration of AIBN in the cavity. While the thermal stability of AIBN was not improved by encapsulation, the thermal stability of the larger analogue AMMVN increased 645 times, attributed to a tighter size fit in the cavity. The reactivity of the radical initiators was restored upon its release from the cage in toluene, as evidenced by the thermal and photochemical polymerisation of methyl methacrylate (Fig. 15).

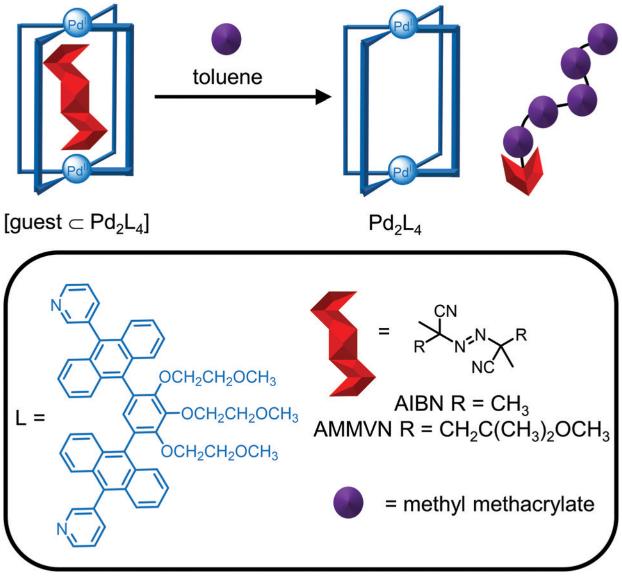

Fig. 15 Stabilisation of radical initiators within a Pd_2L_4 cage reported by Yoshizawa and co-workers. Subsequent release from the cage in toluene restored the reactivity of the radical initiator for the polymerisation of methyl methacrylate.

A new approach in cavity-directed reactions[1] is the use of cages as supramolecular masks to control the regioselectivity of reactions. While the functionalisation of C_{60} leads to complex mixtures of adducts, von Delius, Ribas and co-workers recently reported the formation of the *trans*-3 bis-adduct only from a Bingel cyclopropanation reaction in a ternary complex consisting of a Pd-based tetragonal prismatic cage, [10]cycloparaphenylene ([10]CPP) and C_{60} (Fig. 16).[81] The reaction in the presence of [10]CPP or cage alone gave mixtures of the *trans* and *e*,*e* bis-adducts, respectively, demonstrating the formation of the ternary complex is key to the regioselectivity. The crystal structures of the ternary complexes $[C_{60}\subset[10]CPP\subset Cu^{II}_4L_2L'_4]$ and $[trans\text{-}3\text{-}C_{60}\subset[10]CPP\subset Cu^{II}_4L_2L'_4]$ with the Cu^{II} analogue of the cage provided an explanation for the observed selectivity; although the formation of the *e*,*e* bis-adduct would be expected based on the 90° angle between the cage windows, the tilt of the [10]CPP ring relative to the porphyrin faces of the cage blocks the approach of the dialkyl bromomalonate so that bis-functionalisation occurs at an angle of 120° only. The increased steric bulk from functionalisation resulted in desymmetrisation of the cage signals and a decrease in the binding affinity so that *trans*-3-C_{60} could be removed by solvent washing and addition of C_{60}.

With the increasing number of catalytically active cages, computational studies are providing complementary insights to experimental studies for the improved rational design of catalytic systems. Lusby and co-workers reported the Pd_2L_4 cage (X = N) catalyses Diels–Alder reactions between a bound

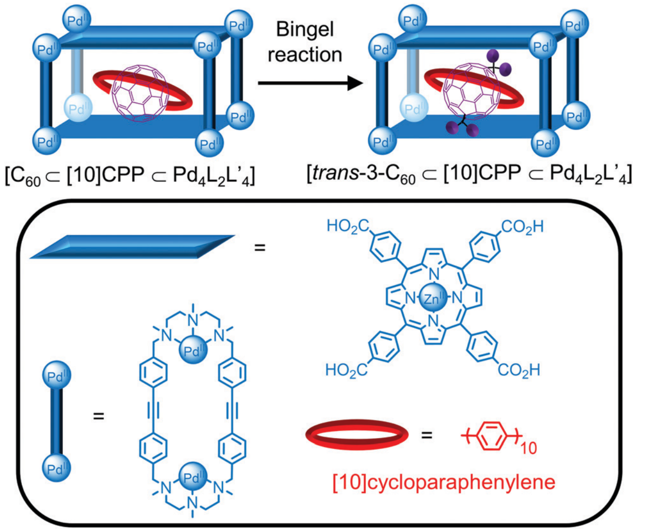

Fig. 16 Regioselective functionalisation of C_{60} reported by von Delius, Ribas and co-workers within a ternary complex consisting of C_{60}, [10]cycloparaphenylene and a $Pd_4L_2L'_4$ cage.

quinone substrate and diene (Fig. 17).[82] Through confinement, the chemoselectivity is reversed so that the smaller but less reactive 1,3-pentadiene reacts preferentially with the bound quinone compared to the larger but more reactive 9,10-dimethylanthracene, unlike the uncatalysed reaction. Furthermore, subtle changes to the cage such as a replacement of a pyridine (X = N) with a benzene ring (X = CH) resulted in no catalytic activity even though the quinone is bound more strongly. Computational studies provided insight into the cause of this change in catalytic activity;[77] although both cages activate the dienophile by lowering the LUMO, the energetic cost to distort the cage for favourable transition state binding was higher for the less flexible cage with X = CH and thus, this cage was not catalytically active. This highlights the synergistic roles experimental and computational studies play in the design of cages for applications and also the need for the development of new computational methods, particularly those that are inexpensive in terms of computational time but accurate.

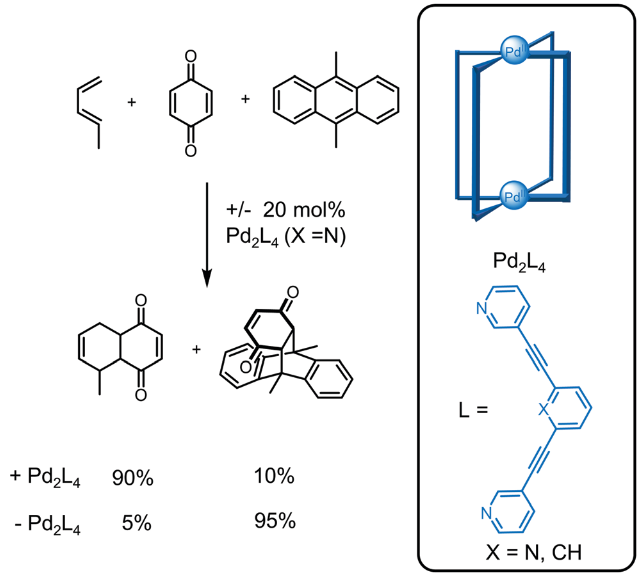

Fig. 17 Catalysis of Diels–Alder reactions by a Pd_2L_4 cage (when X = N) reported by Lusby and co-workers where the chemoselectivity is reversed in comparison to the uncatalysed reaction in the absence of the cage.

5. Conclusions

This Tutorial Review has introduced the different approaches (directional bonding, symmetry interaction and panelling) to the design of metallosupramolecular cages as well as the various factors influencing the self-assembly process from the building block design to the choice of solvent and presence of guests. In many cases, cages can be rationally designed with an understanding of these design principles, however, serendipity can also play a role in the discovery of new and unexpected architectures. In either case, a range of complementary characterisation techniques are necessary to identify the cage, particularly when multiple architectures are possible from the same building blocks.

NMR spectroscopy, mass spectrometry, X-ray crystallography and increasingly computational studies are the workhorses of cage characterisation, each with their strengths and challenges. While NMR spectroscopy and mass spectrometry are primarily used to provide information about the symmetry and composition of the cage, respectively, they can also give insight into the size and shape of the cage and its host–guest complexes through DOSY and ion-mobility mass spectrometry. This information can also be obtained by X-ray crystallography from the three-dimensional structure of the cage. As less computationally expensive but accurate computational methods are being developed to rationalise experimental findings, there is the opportunity to exploit them as prediction tools to facilitate cage design, discovery and application.

From the initial pioneering self-assembly of metallosupramolecular cages, the field has evolved from understanding the fundamentals to applying this knowledge to the design of cages for applications. As the boundaries of self-assembly are pushed and the size and complexity of the cages increase, the toolbox of design principles will be expanded and this will allow not only more complex functionality for applications but also drive the development of new characterisation techniques.

Conflicts of interest

There are no conflicts to declare.

Acknowledgements

Financial support from the Deutsche Forschungsgemeinschaft (DFG, project numbers 413396832 and 429518153) is gratefully acknowledged.

Notes and references

1 M. Yoshizawa, J. K. Klosterman and M. Fujita, *Angew. Chem., Int. Ed.*, 2009, **48**, 3418–3438 and references cited therein.

2 T. K. Ronson, S. Zarra, S. P. Black and J. R. Nitschke, *Chem. Commun.*, 2013, **49**, 2476–2490 and references cited therein.

3 M. Fujita, K. Umemoto, M. Yoshizawa, N. Fujita, T. Kusukawa and K. Biradha, *Chem. Commun.*, 2001, 509–518 and references cited therein.

4 K. Harris, D. Fujita and M. Fujita, *Chem. Commun.*, 2013, **49**, 6703–6712 and references cited therein.

5 Y. Sun, C. Chen, J. Liu and P. J. Stang, *Chem. Soc. Rev.*, 2020, **49**, 3889–3919 and references cited therein.

6 R. Chakrabarty, P. S. Mukherjee and P. J. Stang, *Chem. Rev.*, 2011, **111**, 6810–6918 and references cited therein.

7 D. L. Caulder and K. N. Raymond, *Acc. Chem. Res.*, 1999, **32**, 975–982 and references cited therein.

8 A. Galan and P. Ballester, *Chem. Soc. Rev.*, 2016, **45**, 1720–1737 and references cited therein.

9 Y. Fang, J. A. Powell, E. Li, Q. Wang, Z. Perry, A. Kirchon, X. Yang, Z. Xiao, C. Zhu, L. Zhang, F. Huang and H.-C. Zhou, *Chem. Soc Rev.*, 2019, **48**, 4707–4730 and references cited therein.

10 D. Zhang, T. K. Ronson, Y.-Q. Zou and J. R. Nitschke, *Nat. Rev. Chem.*, 2021, **5**, 168–182 and references cited therein.

11 T. Beissel, R. E. Powers and K. N. Raymond, *Angew. Chem., Int. Ed. Engl.*, 1996, **35**, 1084–1086.

12 R. W. Saalfrank, A. Stark, K. Peters and H. G. von Schnering, *Angew. Chem., Int. Ed. Engl.*, 1988, **27**, 851–853.

13 M. Fujita, D. Oguro, M. Miyazawa, H. Oka, K. Yamaguchi and K. Ogura, *Nature*, 1995, **378**, 469–471.

14 B. Olenyuk, J. A. Whiteford, A. Fechtenkötter and P. J. Stang, *Nature*, 1999, **398**, 796–799.

15 L.-L. Yan, C.-H. Tan, G.-L. Zhang, L.-P. Zhou, J.-C. Bünzli and Q.-F. Sun, *J. Am. Chem. Soc.*, 2015, **137**, 8550–8555.

16 X.-Q. Guo, L.-P. Zhou, S.-J. Hu, L.-X. Cai, P.-M. Cheng and Q.-F. Sun, *J. Am. Chem. Soc.*, 2021, **143**, 6202–6210.

17 Y. Zhou, H. Li, T. Zhu, T. Gao and P. Yan, *J. Am. Chem. Soc.*, 2019, **141**, 19634–19643.

18 E. O. Bobylev, B. de Bruin and J. N. H. Reek, *Inorg. Chem.*, 2021, **60**, 12498–12505.

19 D. Rota Martir and E. Zysman-Colman, *Chem. Commun.*, 2019, **55**, 139–158 and references cited therein.

20 P. R. Symmers, M. J. Burke, D. P. August, P. I. T. Thomson, G. S. Nichol, M. R. Warren, C. J. Campbell and P. J. Lusby, *Chem. Sci.*, 2015, **6**, 756–760.

21 R. Kramer, J. M. Lehn and A. Marquis-Rigault, *Proc. Natl. Acad. Sci. U. S. A.*, 1993, **90**, 5394–5398.

22 W. Cullen, C. A. Hunter and M. D. Ward, *Inorg. Chem.*, 2015, **54**, 2626–2637.

23 A. J. McConnell and M. Lehr, in *Supramolecular Chemistry in Water*, ed. S. Kubik, Wiley-VCH, 2019, pp. 249–284 and references cited therein.

24 E. G. Percástegui, T. K. Ronson and J. R. Nitschke, *Chem. Rev.*, 2020, **120**, 13480–13544 and references cited therein.

25 R. Zhu, J. Lübben, B. Dittrich and G. H. Clever, *Angew. Chem., Int. Ed.*, 2015, **54**, 2796–2800.

26 P. Howlader and P. S. Mukherjee, *Chem. Sci.*, 2016, **7**, 5893–5899.

27 P. Howlader, E. Zangrando and P. S. Mukherjee, *J. Am. Chem. Soc.*, 2020, **142**, 9070–9078.

28 P. Howlader, S. Mondal, S. Ahmed and P. S. Mukherjee, *J. Am. Chem. Soc.*, 2020, **142**, 20968–20972.

29 L.-J. Chen, H.-B. Yang and M. Shionoya, *Chem. Soc. Rev.*, 2017, **46**, 2555–2576 and references cited therein.

30 A. V. Virovets, E. Peresypkina and M. Scheer, *Chem. Rev.*, 2021, **121**, 14485–14554 and references cited therein.

31 S. M. Jansze, M. D. Wise, A. V. Vologzhanina, R. Scopelliti and K. Severin, *Chem. Sci.*, 2017, **8**, 1901–1908.

32 S. M. Jansze, D. Ortiz, F. Fadaei Tirani, R. Scopelliti, L. Menin and K. Severin, *Chem. Commun.*, 2018, **54**, 9529–9532.

33 M. Tominaga, K. Suzuki, M. Kawano, T. Kusukawa, T. Ozeki, S. Sakamoto, K. Yamaguchi and M. Fujita, *Angew. Chem., Int. Ed.*, 2004, **43**, 5621–5625.

34 D. Fujita, Y. Ueda, S. Sato, H. Yokoyama, N. Mizuno, T. Kumasaka and M. Fujita, *Chem*, 2016, **1**, 91–101.

35 Q.-F. Sun, J. Iwasa, D. Ogawa, Y. Ishido, S. Sato, T. Ozeki, Y. Sei, K. Yamaguchi and M. Fujita, *Science*, 2010, **328**, 1144–1147.

36 D. Fujita, Y. Ueda, S. Sato, N. Mizuno, T. Kumasaka and M. Fujita, *Nature*, 2016, **540**, 563.

37 Y. Domoto, M. Abe and M. Fujita, *J. Am. Chem. Soc.*, 2021, **143**, 8578–8582.

38 Y. Domoto, M. Abe, T. Kikuchi and M. Fujita, *Angew. Chem., Int. Ed.*, 2020, **59**, 3450–3454.

39 L. R. Holloway, P. M. Bogie and R. J. Hooley, *Dalton Trans.*, 2017, **46**, 14719–14723 and references cited therein.

40 W. M. Bloch and G. H. Clever, *Chem. Commun.*, 2017, **53**, 8506–8516 and references cited therein.

41 S. Sudan, R.-J. Li, S. M. Jansze, A. Platzek, R. Rudolf, G. H. Clever, F. Fadaei-Tirani, R. Scopelliti and K. Severin, *J. Am. Chem. Soc.*, 2021, **143**, 1773–1778.

42 J. E. M. Lewis and J. D. Crowley, *ChemPlusChem*, 2020, **85**, 815–827 and references cited therein.

43 D. Ogata and J. Yuasa, *Angew. Chem., Int. Ed.*, 2019, **58**, 18424–18428.

44 M. Hardy and A. Lützen, *Chem. – Eur. J.*, 2020, **26**, 13332–13346 and references cited therein.

45 Y.-Y. Zhang, W.-X. Gao, L. Lin and G.-X. Jin, *Coord. Chem. Rev.*, 2017, **344**, 323–344 and references cited therein.

46 L. S. Lisboa, J. A. Findlay, L. J. Wright, C. G. Hartinger and J. D. Crowley, *Angew. Chem., Int. Ed.*, 2020, **59**, 11101–11107.

47 N. Geue, R. E. P. Winpenny and P. E. Barran, *Chem. Soc. Rev.*, 2022, **51**, 8–27 and references cited therein.

48 L. Avram and Y. Cohen, *Chem. Soc. Rev.*, 2015, **44**, 586–602 and references cited therein.

49 Y. Cohen, S. Slovak and L. Avram, *Chem. Commun.*, 2021, **57**, 8856–8884 and references cited therein.

50 L. Avram and A. Bar-Shir, *Org. Chem. Front.*, 2019, **6**, 1503–1512 and references cited therein.

51 Y. Tsujimoto, T. Kojima and S. Hiraoka, *Chem. Sci.*, 2014, **5**, 4167–4172.

52 Y. Matsumura, S. Hiraoka and H. Sato, *Phys. Chem. Chem. Phys.*, 2017, **19**, 20338–20342.

53 M. Foroozandeh, G. A. Morris and M. Nilsson, *Chem. – Eur. J.*, 2018, **24**, 13988–14000.

54 M. Lehr, T. Paschelke, E. Trumpf, A.-M. Vogt, C. Näther, F. D. Sönnichsen and A. J. McConnell, *Angew. Chem., Int. Ed.*, 2020, **59**, 19344–19351.

55 M. P. Crockett, H. Zhang, C. M. Thomas and J. A. Byers, *Chem. Commun.*, 2019, **55**, 14426–14429.

56 S. Turega, M. Whitehead, B. R. Hall, A. J. H. M. Meijer, C. A. Hunter and M. D. Ward, *Inorg. Chem.*, 2013, **52**, 1122–1132.

57 A. J. McConnell, C. M. Aitchison, A. B. Grommet and J. R. Nitschke, *J. Am. Chem. Soc.*, 2017, **139**, 6294–6297.

58 L. L. K. Taylor, I. J. Vitorica-Yrezabal, I. Borilović, F. Tuna and I. A. Riddell, *Chem. Commun.*, 2021, **57**, 11252–11255.

59 P. Thordarson, *Chem. Soc. Rev.*, 2011, **40**, 1305–1323 and references cited therein.

60 P. C. M. van Zijl and N. N. Yadav, *Magn. Reson. Med.*, 2011, **65**, 927–948 and references cited therein.

61 M. Yamashina, Y. Tanaka, R. Lavendomme, T. K. Ronson, M. Pittelkow and J. R. Nitschke, *Nature*, 2019, **574**, 511–515.

62 M. D. Pluth, B. E. F. Tiedemann, H. van Halbeek, R. Nunlist and K. N. Raymond, *Inorg. Chem.*, 2008, **47**, 1411–1413.

63 K. Du, S. D. Zemerov, S. Hurtado Parra, J. M. Kikkawa and I. J. Dmochowski, *Inorg. Chem.*, 2020, **59**, 13831–13844.

64 K. Du, S. D. Zemerov, P. J. Carroll and I. J. Dmochowski, *Inorg. Chem.*, 2020, **59**, 12758–12767.

65 D. P. Weimann, M. Kogej and C. A. Schalley, in *Analytical Methods in Supramolecular Chemistry*, ed. C. A. Schalley, Wiley VCH, 2012 and references cited therein.

66 Z. Qi, T. Heinrich, S. Moorthy and C. A. Schalley, *Chem. Soc. Rev.*, 2015, **44**, 515–531 and references cited therein.

67 S. Sakamoto, M. Fujita, K. Kim and K. Yamaguchi, *Tetrahedron*, 2000, **56**, 955–964.

68 E. Kalenius, M. Groessl and K. Rissanen, *Nat. Rev. Chem.*, 2019, **3**, 4–14 and references cited therein.

69 O. H. Lloyd Williams and N. J. Rijs, *Front. Chem.*, 2021, **9**, DOI: 10.3389/fchem.2021.682743 and references cited therein.

70 S. P. Black, A. R. Stefankiewicz, M. M. J. Smulders, D. Sattler, C. A. Schalley, J. R. Nitschke and J. K. M. Sanders, *Angew. Chem., Int. Ed.*, 2013, **52**, 5749–5752.

71 K. E. Ebbert, L. Schneider, A. Platzek, C. Drechsler, B. Chen, R. Rudolf and G. H. Clever, *Dalton Trans.*, 2019, **48**, 11070–11075.

72 K. Rissanen, *Chem. Soc. Rev.*, 2017, **46**, 2638–2648 and references cited therein.

73 A. W. Markwell-Heys, M. L. Schneider, J. M. L. Madridejos, G. F. Metha and W. M. Bloch, *Chem. Commun.*, 2021, **57**, 2915–2918.

74 C. G. P. Taylor, S. P. Argent, M. D. Ludden, J. R. Piper, C. Mozaceanu, S. A. Barnett and M. D. Ward, *Chem. – Eur. J.*, 2020, **26**, 3054–3064.

75 M. Hoshino, A. Khutia, H. Xing, Y. Inokuma and M. Fujita, *IUCrJ*, 2016, **3**, 139–151 and references cited therein.

76 T. A. Young, R. Gheorghe and F. Duarte, *J. Chem. Inf. Model.*, 2020, **60**, 3546–3557.

77 T. A. Young, V. Martí-Centelles, J. Wang, P. J. Lusby and F. Duarte, *J. Am. Chem. Soc.*, 2020, **142**, 1300–1310.

78 A. Tarzia, J. E. M. Lewis and K. E. Jelfs, *Angew. Chem., Int. Ed.*, 2021, **60**, 20879–20887.

79 W. Cullen, S. Turega, C. A. Hunter and M. D. Ward, *Chem. Sci.*, 2015, **6**, 2790–2794.

80 M. Yamashina, Y. Sei, M. Akita and M. Yoshizawa, *Nat. Commun.*, 2014, **5**, 4662.

81 E. Ubasart, O. Borodin, C. Fuertes-Espinosa, Y. Xu, C. García-Simón, L. Gómez, J. Juanhuix, F. Gándara, I. Imaz, D. Maspoch, M. von Delius and X. Ribas, *Nat. Chem.*, 2021, **13**, 420–427.

82 V. Martí-Centelles, A. L. Lawrence and P. J. Lusby, *J. Am. Chem. Soc.*, 2018, **140**, 2862–2868.